I&EC research
Industrial & Engineering Chemistry Research

pubs.acs.org/IECR
Article

Understanding Strain Effects on IrO_2 for Oxygen Evolution Electrocatalysis

Published as part of Industrial & Engineering Chemistry Research special issue "Celebrating Undergraduate Research in Chemical Engineering 2024".

Erum Hassan,[†] S. A. Keishana Navodye,[†] and G. T. Kasun Kalhara Gunasooriya*

Cite This: *Ind. Eng. Chem. Res.* 2025, 64, 16531−16543

Read Online

ACCESS | Metrics & More | Article Recommendations | Supporting Information

ABSTRACT: Understanding how strain influences the electronic and geometric properties of surface active sites and the activity and stability of the iridium oxide-catalyzed oxygen evolution reaction (OER) has significant scientific and technological implications for designing next-generation electrocatalysts. In this study, we use density functional theory (DFT) calculations to systematically investigate the effect of compressive and tensile biaxial surface strains on the OER activity and stability of the IrO_2(110), IrO_2(100), and IrO_2(101) surfaces. Our results reveal significant changes in the adsorption free energies of the OER intermediates due to strain, which in turn influences the OER activity. Furthermore, we evaluate how the electronic structure of IrO_2 surface atoms varies with strain, leading to a fundamental theoretical understanding of strain effects. Our theoretical analysis further accounts for the effects of strain in the presence of a nearby surface Ir vacancy and high surface oxygen coverage, representing realistic surfaces under OER conditions. This work expands the current understanding of strain-assisted activity and stability enhancements in OER catalysts, paving the way for the development of strain-engineered electrocatalysts.

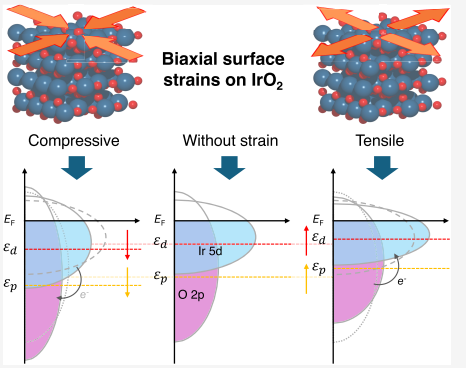

1. INTRODUCTION

Green hydrogen production from water electrolyzers ($2H_2O \rightarrow 2H_2 + O_2$) offers a promising avenue for reducing global reliance on fossil fuels and achieving the growing demand for sustainable fuels and chemical production.[1,2] Proton exchange membrane (PEM)-based acidic water electrolyzers have gained significant scientific attention due to various advantages over alkaline water electrolyzers, such as the ability to achieve higher current densities, high product purity, low operating pressure and temperature, and fast system response rates.[3] IrO_2 is the current state-of-the-art catalyst for the anodic oxygen evolution reaction (OER), whereas Pt-based catalysts are widely used for the cathodic hydrogen evolution reaction (HER). However, widespread utilization of acidic water electrolyzers is hampered primarily by the high operating overpotentials induced by the sluggish kinetics of the anodic OER, reducing the energy efficiency of the overall conversion process and the high costs of Ir-based electrode materials.[1,2] In order to overcome these constraints, it is imperative to identify potential pathways to enhance the intrinsic OER activity and stability, thus effectively utilizing precious IrO_2 as the anode catalytic material.

Strain engineering is a commonly used strategy to tune the electronic structure of surface atoms among many other methods, such as alloying, heteroatom doping, introducing defects, and manipulating morphology and granularity.[4,5] Applying strain to a catalyst surface alters the bond lengths between surface atoms, which can systematically modulate the electronic structure of the active sites. This modification in the electronic structure of the active site is used to optimize the adsorption strengths of reactants, intermediates, and products, thus facilitating more favorable bond formations and breakages by potentially lowering the reaction barriers and improving the selectivity of the desired products.[6,7] The lattice strain is defined as the deviation from the equilibrium spacing between atoms in the crystal lattice and can be either compressive or tensile. Strain (ε) is calculated as the difference in the atom−atom bond distance due to the strained and unstrained system, normalized to the unstrained atom−atom bond distance, i.e., $\varepsilon = (d-d_s)/d_s$, where d is the atom−atom bond distance under strain, and d_s is the atom−atom bond distance of the unstrained system.[5,8]

Received: March 23, 2025
Revised: July 3, 2025
Accepted: July 15, 2025
Published: August 15, 2025

https://doi.org/10.1021/acs.iecr.5c01104
Ind. Eng. Chem. Res. 2025, 64, 16531−16543

Typically, strains are introduced by creating a lattice mismatch at the interface between two materials and altering the bond lengths between atoms via size and shape variations, introducing defects, alloying, etc.[4,5,9] Experimentally, materials with core and shell structures are widely used for the applications of strain due to the differences in lattice parameters of the core and shell that result in a change in the lattice shape at the interface.[10−12] The material with the smaller lattice constant generally experiences tensile strain, while the material with the larger lattice constant is under compression in these core−shell structures.[13] The epitaxial growth technique is a widely used method to fabricate materials with core−shell structures with oriented growth between two crystalline materials.[14] The interface of epitaxially grown materials is under either maximum compressive or tensile strain, depending on the lattice parameter mismatch, and diminishes with increasing distance from the interface.[15]

Strain engineering has been widely explored to optimize the performance of the OER on IrO_2 surfaces. Meng et al.[16] manipulated the lattice strain of IrO_x on IrCo nanodendrites by varying the number of IrO_x atomic layers deposited on IrCo. In their work, approximately two atomic layers of IrO_x resulted in a 2.51% compressive strain, and the subsequent increase in atomic layers up to nine completely diminished the compressive strain on IrO_x. Three-layered IrO_x with 1.51% compressive strain showed optimum OER performance with an overpotential of 247 mV at a current density of 10 mA cm^{-2}. Theoretical modeling of the IrO_x layers on IrCo was performed by changing the lattice constants of the unstrained $IrO_2(110)$ surface to apply compressive strains parallel to the surface. Sun et al.[17] varied the annealing temperature during catalyst synthesis to modulate the strain on IrO_2 electrocatalysts, where decreasing the annealing temperature led to an increase in the a and b axes and resulted in a contraction along the *c*-axis of IrO_2, thereby decreasing the c/a ratio. Samples with lower c/a ratios were observed to have higher deviations from the standard IrO_2, increasing the lattice strain in the system, which resulted in higher OER activity. Hao et al.[18] incorporated torsion strain into $IrO_{2-\delta}$ by fast pyrolysis synthesis and doping of Tm and Ta, resulting in abundant trigeminal grain boundaries in the material. The resultant $Ta_{0.1}Tm_{0.1}Ir_{0.8}O_{2-\delta}$ catalyst exhibited superior activity for the OER, with a low overpotential of 198 mV at 10 mA cm^{-2}. Torsion strain along the grain boundaries of the nanocrystalline domains resulted in altering the Ir−O bond lengths, subsequently leading to modifications in the adsorption strengths of OER intermediates and lower energy barriers for the OER. Moreover, Wu et al.[19] demonstrated that a nanocatalyst of IrO_x supported on a $Sb_{0.3}Ir_{0.7}O_x$ core outperformed the mass activity of commercial IrO_2 by roughly 26 times. This core−shell-type catalyst contained twin boundaries at the interface of the crystalline grains with both shear and axial strains. The Ir 5d-band center was upshifted toward the Fermi level, and Ir−O bond lengths of the catalyst surface were modified by this bidirectional strain induced by grain boundaries and doping of Sb in the core, thereby becoming more active for the OER. Additionally, localized Ir atoms supported at the surface cation sites on tensile-strained MnO_2 showed enhanced OER activity due to the increase of favorability for the LOM mechanism.[20] In situ synchrotron radiation infrared (SRIR) spectroscopy and X-ray adsorption fine structure (XAFS) revealed that O* adsorbed on Ir quickly reacts with adjacent lattice O to form O_2, creating a surface oxygen vacancy. The oxygen vacancy reacts immediately with water molecules to fill the vacancy, enhancing the OER activity and catalyst stability. In addition to catalyst activity, catalyst stability is also affected by the presence of strain. Recent theoretical work led by Alexandrov and co-workers revealed that moderate compressive strains (−2%) on the (110) surfaces resulted in a significant decrease in the surface metal vacancy formation barriers on IrO_2 and RuO_2, promoting transition metal dissolution.[7] Although a considerable number of studies focused on the current state-of-the-art IrO_2 electrocatalysts, a comprehensive theoretical study understanding strain effects on surfaces other than $IrO_2(110)$, under surface Ir vacancy and high surface oxygen coverage conditions, which are more realistic to prevail under operating OER conditions, remains underexplored.

This study is motivated by our interest in establishing a fundamental relationship between surface strain and OER activity and stability on IrO_2 catalysts using density functional theory (DFT) calculations. First, based on a comprehensive surface energy analysis and Wulff diagram construction, we identified the thermodynamically most stable low Miller-index IrO_2 surfaces: $IrO_2(110)$, $IrO_2(101)$, and $IrO_2(100)$. Next, we evaluated the effects of strain on OER activity by calculating the adsorption free energies of OER intermediates using both the adsorbate evolving mechanism (AEM) and lattice oxygen mechanism (LOM) on clean IrO_2 surfaces. The electronic structure modifications of IrO_2 surfaces under different strain conditions were analyzed by using the density of states (DOS) and Bader charges. Then, we systematically extended our study to analyze the OER activity in the presence of a nearby Ir vacancy and under high surface oxygen coverage conditions, which resemble practical OER operating conditions. The improved understanding based on these theoretical findings unravels the relationship between the electrocatalytic activity and stability and the strain on different IrO_2 surfaces, leading to a more efficient design of electrochemical conversion systems.

2. COMPUTATIONAL METHODS

Periodic spin-polarized DFT calculations were performed using the Perdew−Burke−Ernzerhof (PBE) exchange-correlation functional,[21] a plane-wave basis set with a cutoff kinetic energy of 500/400 eV for bulk/surface structures, and the projector-augmented wave (PAW) method, as implemented in the Vienna Ab initio Simulation Package (VASP version 5.4.1).[22,23] The electronic convergence criterion was 10^{-5} eV, while the force criterion for geometry relaxation was 0.05 eV $Å^{-1}$. The most stable phase of IrO_2 with the $P4_2/mnm$ (rutile) space group (see Figure S1a) was selected as the IrO_2 bulk structure for the analysis, and our DFT-PBE optimized lattice parameters were $a = b = 4.54$ Å and $c = 3.19$ Å. Using the bulk structure, we generated surfaces with various Miller indices and the surface energy (J/m^2) for a given facet was calculated based on eq 1,

$$\text{surface energy} = \frac{E_{\text{surface}} - n \times E_{\text{bulk}}}{(2 \times \text{SA})} \times 16.01 \quad (1)$$

where E_{surface} and E_{bulk} represent the DFT electronic energies of the considered surface and bulk unit cell of IrO_2, respectively, and n and SA are the ratio of the number of atoms in the surface cell to the bulk unit cell and the calculated surface area of the surface unit cell, respectively. Based on our surface

https://doi.org/10.1021/acs.iecr.5c01104
Ind. Eng. Chem. Res. 2025, 64, 16531−16543

energy analysis, we selected the (110), (101), and (100) terminations of IrO_2, which resulted in the lowest surface energy (see Section 3.1). The IrO_2(110) and IrO_2(101) oxide surfaces were modeled with (2 × 1) with a 4-layer slab, whereas IrO_2(100) was modeled with a (2 × 2) unit cell with the same number of atomic layers. The surface slabs were separated in the perpendicular *z*-direction by 15 Å of vacuum, and a dipole correction was applied. To obtain numerically converged results, the Brillouin zone was sampled with (3 × 3 × 1), (2 × 4 × 1), and (3 × 2 × 1) Γ-centered k-point grids for the (110), (101), and (100) surfaces, respectively. A detailed benchmark study on DFT settings is provided in Supporting Information (Computational Methods Benchmarking) and Tables S1, S2.

Uniform biaxial surface strains ranging from −5 to 5% in intervals of 1% were applied in the *x* and *y* directions, and all atomic layers of the surface models were allowed to relax without constraining any atomic positions. Negative surface strain values indicate compressive strain, while positive values indicate tensile strain. The percentage of strain indicates the percentage change in the *x* and *y* dimensions of the surface cell. It is important to note that the application of biaxial surface strain in this study differs from that of bulk strain. In the case of bulk strain calculations, strain is applied to the entire bulk structure first, and then surface models are created. In contrast, for uniform biaxial surface strain calculations, surface models are generated from the unstrained bulk structure, after which the surface strain is applied. In all of the surface calculations, the bottom half of the slabs in the vertical z-direction were constrained at the preoptimized positions under different strains, while the top half of the slab and the adsorbed species, if present, were fully relaxed. All crystal structure manipulations and data analysis were carried out using the Python Materials Genomics package[24] and the Atomic Simulation Environment (ASE).[25] Atomic charges were calculated using Bader analysis, as implemented by Henkelman et al.[26] Effective Bader charges are defined as $q = Z_{val} - q_{Bader}$, where Z_{val} is the number of valence electrons and q_{Bader} is the computed Bader charge.

The OER activities of the different surfaces with varying strains were evaluated based on the theoretical overpotential (η) and considering both the adsorbate evolving mechanism (AEM) and the lattice oxygen mechanism (LOM). The four proton-coupled electron transfer (PCET) reactions under acidic conditions for the 4e$^-$ AEM OER mechanism are

$$H_2O_{(l)} + * \rightarrow OH^* + (H^+ + e^-) \quad (2)$$

$$OH^* \rightarrow O^* + (H^+ + e^-) \quad (3)$$

$$H_2O_{(l)} + O^* \rightarrow OOH^* + (H^+ + e^-) \quad (4)$$

$$OOH^* \rightarrow O_{2(g)} + * + (H^+ + e^-) \quad (5)$$

Reactions 2 and 3 are similar for the LOM, while reactions 4 and 5 involve a nearby lattice oxygen according to the following reactions

$$O^* + O_{lattice} \rightarrow O_{2(g)} + V_o \quad (6)$$

$$V_o + H_2O \rightarrow H^*_{lattice-O} + (H^+ + e^-) \quad (7)$$

$$H^*_{lattice-O} \rightarrow * + (H^+ + e^-) \quad (8)$$

Here, V_o represents the oxygen vacancy adjacent to the active metal site on the surface.

The computational hydrogen electrode (CHE) was used to express the chemical potential of the proton−electron pair ($H^+ + e^-$), which relates the chemical potential of the proton−electron pair with the chemical potential of the gas-phase H_2 molecule based on the equilibrium $\mu[H^+] + \mu[e^-] = \frac{1}{2}\mu[H_{2(g)}]$ at 0 V_{RHE} (where RHE is the reversible hydrogen electrode) and corrects the driving force with the deviation of the applied potential from equilibrium.[27] To avoid using the O_2 electronic energy, which is difficult to determine accurately within standard GGA-DFT, the experimental free energy of $2H_2O \rightarrow O_2 + 2H_2$, $\Delta G = 4.92$ eV, was used. Therefore, the Gibbs free energies of reactions 2−5 depend on the adsorption free energies of the reaction intermediates (ΔG_{O^*}, ΔG_{OH^*}, and ΔG_{OOH^*}). The adsorption free energies of these reaction intermediates are calculated as $\Delta G_{adsorption} = \Delta E_{DFT} + \Delta E_{ZPE} + \int_0^{298.15} \Delta C_p dT - T\Delta S$ with respect to the catalyst surface, relative to H_2O(g) and H_2(g) at U = 0 V and standard conditions (T = 298.15 K, P = 1 bar, and pH = 0). In this equation, ΔE_{DFT} is the difference in DFT-calculated electronic energies; ΔE_{ZPE} is the difference in zero-point energies; $\int_0^{298.15} \Delta C_p dT$ is the difference in integrated heat capacity from 0 to 298.15 K, and ΔS is the change in entropy of the adsorbed species. The values for the current analysis were taken from a previous study by Navodye and Gunasooriya.[28]

The theoretical thermodynamic OER overpotential (η_{OER}), which is a measure of the activity of a catalyst, is then defined from the Gibbs free energies of reactions 2−5 for the AEM mechanism ($\eta_{OER\text{-}AEM}$)

$$\eta_{OER-AEM}(V) = \max[\Delta G_{OH^*}, \Delta G_{O^*} - \Delta G_{OH^*}, \Delta G_{OOH^*} - \Delta G_{O^*}; 4.92 - \Delta G_{OOH^*}]/e - 1.23V \quad (9)$$

while the Gibbs free energies of reactions 2,3,6−8 were used to define the LOM mechanism ($\eta_{OER\text{-}LOM}$)

$$\eta_{OER-LOM}(V) = \max[\Delta G_{OH^*}, \Delta G_{O^*} - \Delta G_{OH^*}, 4.92 + \Delta G_{H^*} - \Delta G_{O^*}, -\Delta G_{H^*}]/e - 1.23V \quad (10)$$

The step with the largest value in eq 9 for the AEM and eq 10 for LOM is referred to as the potential-determining step (PDS) for the OER. It is important to note that η should not be compared directly with a measured overpotential since the measured overpotential depends on the current density.[2]

3. RESULTS AND DISCUSSION

3.1. Analysis of the IrO_2 Surface Energy and Wulff Shape Construction. To identify the most thermodynamically dominant surfaces and predict the equilibrium shape of an unstrained IrO_2 nanoparticle, we conducted a comprehensive surface energy analysis and constructed a Wulff crystal shape. Surface energies were calculated for all the facets up to a Miller index of 2. For each facet, multiple surfaces with different O-atom-terminated, Ir-terminated, and both Ir- and O-terminated facets were generated, as shown in Figure S1b. We considered all of these surfaces in our surface energy analysis. It is important to note that we preserved IrO_2 stoichiometry and used DFT-optimized lattice parameters while generating

https://doi.org/10.1021/acs.iecr.5c01104
Ind. Eng. Chem. Res. 2025, 64, 16531−16543

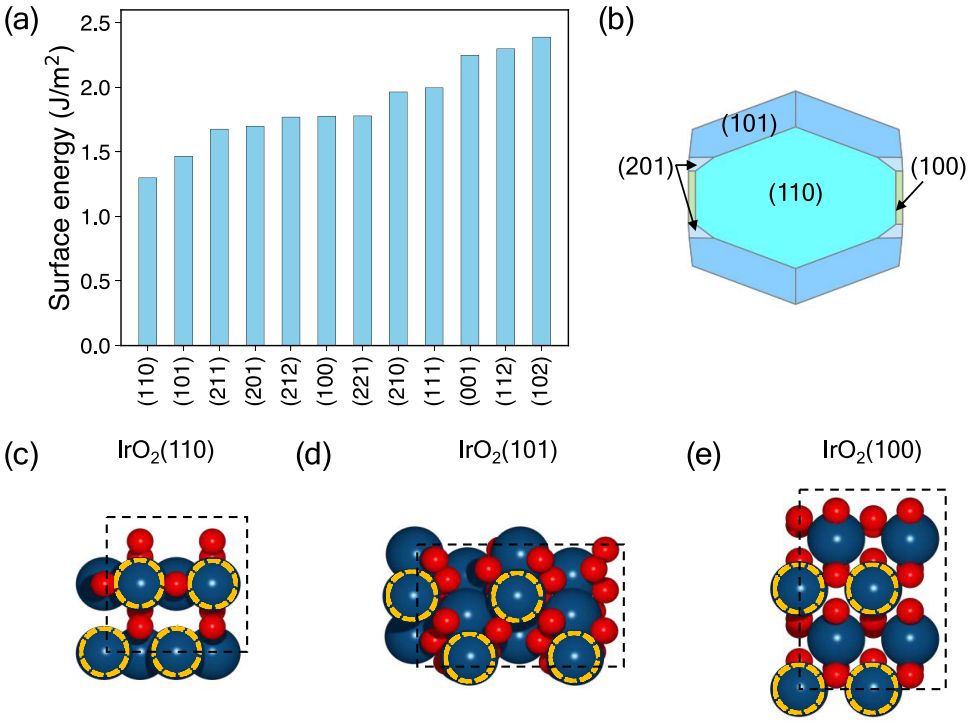

Figure 1. Surface energy analysis of rutile-IrO_2 (space group: tetragonal $P4_2/mnm$) and atomic structures of the facets selected for the study. (a) Surface energies of the facets up to a Miller index of 2, (b) Wulff crystal shape construction based on the surface energy analysis. Top views of the (c) $IrO_2(110)$, (d) $IrO_2(101)$, and (e) $IrO_2(100)$ facets considered in this study. Yellow dotted circles show the surface Ir atoms on each surface, and black dashed lines denote the surface unit cells. Color code: Ir, blue; O, red.

unstrained surfaces for this analysis. Figure 1a shows the calculated surface energy of the most stable surface for a given Miller index. A lower surface energy indicates a higher propensity for the formation of chemical bonds, thus suggesting a thermodynamic preference for crystal growth along a specific plane. Based on our analysis, $IrO_2(110)$ is the most thermodynamically stable facet, with a surface energy of 1.30 J/m^2 in alignment with previous studies.[29,30] $IrO_2(101)$ showed the next highest stability with a surface energy of 1.47 J/m^2, followed by the higher Miller index facets of $IrO_2(211)$, $IrO_2(201)$, and $IrO_2(212)$ with surface energies of 1.68, 1.70, and 1.77 J/m^2, respectively. The remaining low Miller index facets $IrO_2(100)$, $IrO_2(111)$, and $IrO_2(001)$ appeared to be relatively less stable, with surface energies of 1.78, 2.00, and 2.25 J/m^2, respectively. Subsequently, based on the surface energy analysis, a Wulff crystal shape diagram (Figure 1b) was constructed to represent the thermodynamically stable crystal shape of the IrO_2 nanoparticles. $IrO_2(110)$ and $IrO_2(101)$ are the most dominant facets of IrO_2, significantly covering the surface with area fractions of 48.7 and 48.2%, respectively. Additionally, $IrO_2(201)$ and $IrO_2(100)$ cover minor surface area fractions of 1.84 and 1.25%, respectively. All other facets, including $IrO_2(211)$, which is the third most stable, do not appear in the Wulff shape, indicating near-zero surface area fractions. The average surface energy of the particle is 1.39 J/m^2, and the shape factor of the particle is 5.36. This calculated shape factor serves as a general measure of anisotropy under equilibrium conditions.

Based on the surface energy analysis and Wulff crystal shape construction, the $IrO_2(110)$ and $IrO_2(101)$ surfaces were initially selected for understanding the effect of surface strain on the OER activity, as these surfaces are the most stable facets with significant surface area fractions. We further included low Miller index $IrO_2(100)$ in the current analysis, although it shows a minor surface area fraction in our analysis. Figure 1c–e shows top views of the considered low Miller index facets of unstrained $IrO_2(110)$, $IrO_2(101)$, and $IrO_2(100)$, respectively. The $IrO_2(110)$ surface comprises two distinct surface Ir sites: a coordinatively unsaturated (CUS) site, where the Ir atom is connected to five oxygen atoms (5c-M), and a bridge site connected to six oxygen atoms (6c-M).[31] In contrast, the $IrO_2(101)$ and $IrO_2(100)$ surfaces feature identical Ir surface sites connected to five oxygen atoms. Subsequently, biaxial surface strains ranging from −5 to 5% with intervals of 1% were applied equally in both the x and y directions in these surface slabs. Negative surface strain values (−5 to −1%) indicate compressive strains, while positive values (1 to 5%) indicate tensile strains. Initially, the atomic structures of pristine surfaces were relaxed without constraining any atomic positions in order to understand the variation of atomic layer distances in the z-direction. Figure S2 shows the variation in the average layer distance with applied strain for the considered IrO_2 surfaces. The average height of a given atomic layer was calculated by considering the z coordinates of all of the Ir atoms in that layer, and the average layer distance was estimated by taking the average of the 3 individual layer distances for a given surface structure. The average layer distance is highest in $IrO_2(110)$ (3.20 Å without strain) and lowest in $IrO_2(100)$ (2.30 Å without strain), while $IrO_2(101)$ shows an intermediate average layer distance of 2.60 Å at 0% strain. For all surfaces, the average layer distance increased with increasing compressive strain, while it decreased with increasing tensile strain, as observed in the experiments.[17,32,33] $IrO_2(110)$ showed the least variation in the average layer distance by decreasing 0.19 Å (5.8% compared to the average layer distance at 0% strain) when considering the −5 to 5%

https://doi.org/10.1021/acs.iecr.5c01104
Ind. Eng. Chem. Res. 2025, 64, 16531−16543

strain range. In contrast, changing strains from −5 to 5% resulted in 0.25 Å (9.5%) and 0.35 Å (15.3%) decrease in $IrO_2(101)$ and $IrO_2(100)$, respectively. Interestingly, the selected IrO_2 surfaces result in different responses under the same range of strain.

3.2. Strain Effects on the Adsorption of OER Intermediates and OER Overpotentials under Low Coverage Conditions. Figure 2 shows the adsorption energies of commonly used OER intermediates on $IrO_2(110)$, $IrO_2(101)$, and $IrO_2(100)$ surfaces with varying biaxial strains under low surface coverage conditions (see Figure S3 for atomistic figures of OH adsorption). As expected, the three surfaces without strain exhibit a range of adsorption energies for all OER intermediates, indicating variations in their local active site moieties. For example, the adsorption free energies of OH (ΔG_{OH*}) are 0.04, 0.26, and 0.14 eV on the $IrO_2(110)$, $IrO_2(101)$, and $IrO_2(100)$ surfaces, respectively. Overall, the adsorption of OER intermediates on $IrO_2(101)$ is the weakest, whereas the strongest adsorption occurs on $IrO_2(110)$. Note that stronger adsorption corresponds to more negative free energy values. The free energy of adsorption of O (ΔG_{O*}) shows a monotonic increase in adsorption strength on the $IrO_2(101)$ surface in a narrow range (1.82−1.73 eV) when the strain is varied from −5 to +5%. Similarly, the ΔG_{O*} on $IrO_2(110)$ is much less sensitive to strain, with a variation in a narrow range of 1.45−1.48 eV. Interestingly, ΔG_{O*} on the $IrO_2(100)$ surface decreases and becomes more favorable when changing the strain from −5 to 1%, remains almost the same at 1−3%, and then increases when the tensile strain is further increased. Moreover, ΔG_{O*} on $IrO_2(100)$ varies in a much wider range (1.40−1.68 eV) compared to the $IrO_2(101)$ and $IrO_2(110)$ surfaces. The free energy of adsorption of OH (ΔG_{OH*}) and OOH (ΔG_{OOH*}) on $IrO_2(100)$ shows a similar trend to ΔG_{O*}, going through a minimum of around 1−3% strain. In contrast to the almost insensitive ΔG_{O*} variation on $IrO_2(110)$ with strain, ΔG_{OH*} on $IrO_2(110)$ shows a monotonic increase in a moderate range of −0.10 to 0.10 eV when changing the strain from −5 to 5%, although ΔG_{OOH*} varies in a narrow range. On $IrO_2(101)$, ΔG_{OH*} is less sensitive to strain, and ΔG_{OOH*} monotonically decreases from 3.52 to 3.31 eV when changing the strain from −5 to 5%.

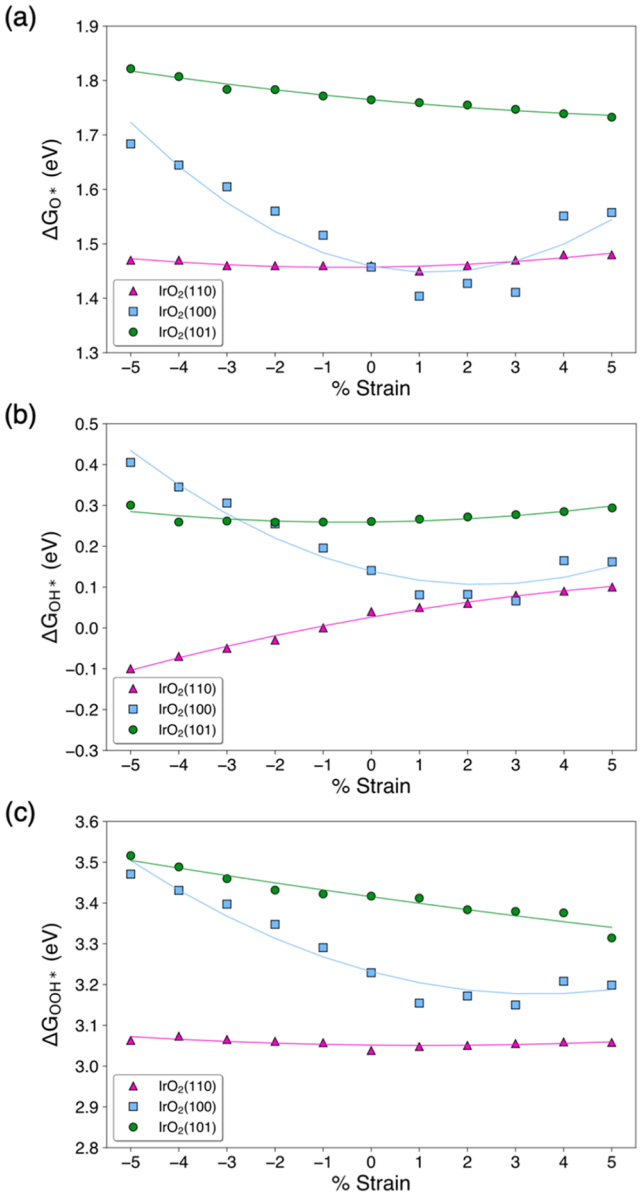

Figure 2. Effect of strain on the adsorption of key OER intermediates. Variation of adsorption free energies of key OER intermediates: (a) O*, (b) OH*, and (c) OOH* adsorption on Ir active sites as a function of strain% on three different facets: $IrO_2(110)$, $IrO_2(100)$, and $IrO_2(101)$. Positive strain values correspond to tensile strain, while negative values indicate compressive strain.

It is well established that the $\Delta G_{adsorption}$ of the OER reaction intermediates follows linear scaling relations since all the intermediates (OH*, O*, and OOH*) adsorb on the surface active sites through an O atom.[2,29,34] Figure S4 shows the scaling relations of ΔG_{OOH*} vs ΔG_{OH*} and ΔG_{O*} and ΔG_{OH*} for IrO_2 surfaces with strain. Overall, the scaling relation of ΔG_{OOH*} vs ΔG_{OH*} with applied strain generally fits within the universal scaling of $\Delta G_{OOH*} = \Delta G_{OH*} + 3.2 \pm 0.4$ eV. However, it is important to note that the ΔG_{OOH*} and ΔG_{OH*} values for the $IrO_2(100)$ surface align well with universal scaling, whereas variation in the ΔG_{OOH*} and ΔG_{OH*} values on the $IrO_2(110)$ and $IrO_2(101)$ surfaces shows no clear trend. The free energies of ΔG_{O*} and ΔG_{OH*} on the IrO_2 surfaces follow a scaling relation of $\Delta G_{O*} = 0.88\Delta G_{OH*} + 1.45$. Similar to the previously observed trend, scaling between O* and OH* aligns well with $IrO_2(100)$, whereas it tends to deviate locally without a clear trend on the $IrO_2(110)$ and $IrO_2(101)$ surfaces.

To evaluate the OER activity on strained surfaces, we considered both the adsorbate evolving mechanism (AEM) and lattice oxygen mechanism (LOM) (see Computational Methods). The AEM mechanism involves only surface OER intermediates, while the LOM mechanism involves both surface and lattice O species. Specifically, the LOM mechanism involves H* adsorption on the lattice oxygen adjacent to the Ir active sites instead of OOH* formation in the AEM, as shown in reactions 7 and 8, respectively. Since the free energy of lattice oxygen vacancy formation ($\Delta G_{O\text{-vacancy}}$) scales with the free energy of H* on the lattice O (ΔG_{H*}),[34,35] we evaluated both the ΔG_{H*} and $\Delta G_{O\text{-vacancy}}$ variations as a function of the applied strain on different surfaces (Figure 3a,b). The H* adsorption is strongest on the $IrO_2(100)$ surface, followed by $IrO_2(101)$ and $IrO_2(110)$ surfaces for all of the strain values. This observed trend of ΔG_{H*} variation with strain is different from the generally observed adsorption strength trend of the OER intermediates, $IrO_2(110) > IrO_2(100) > IrO_2(101)$.

https://doi.org/10.1021/acs.iecr.5c01104
Ind. Eng. Chem. Res. 2025, 64, 16531−16543

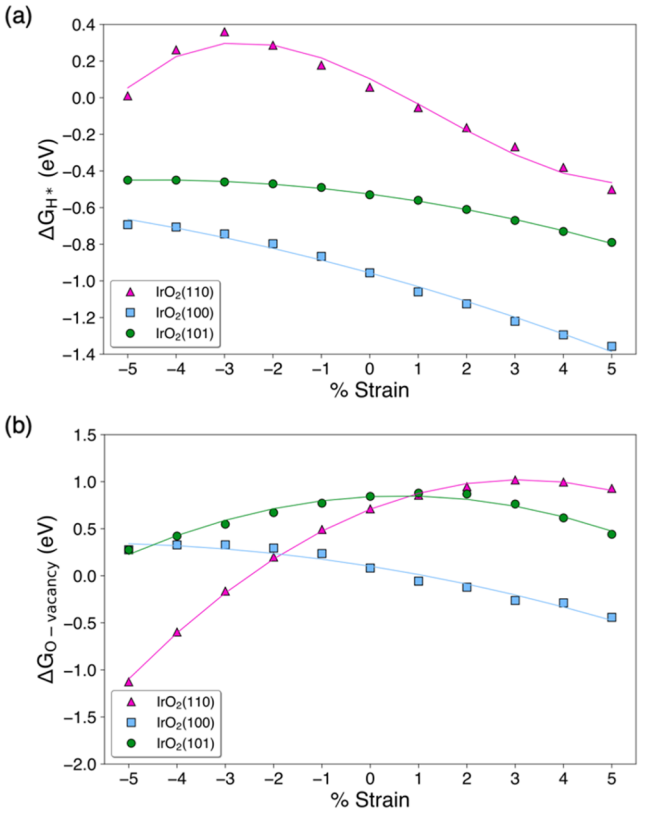

Figure 3. Effect of strain on adsorption free energies of H on lattice O (ΔG_H) and oxygen vacancy formation ($\Delta G_{O\text{-vacancy}}$). (a) ΔG_H and (b) $\Delta G_{O\text{-vacancy}}$ as a function of strain% % on IrO_2 (110), IrO_2 (100), and IrO_2 (101). Note that the oxygen atom that is removed to form an O vacancy is the same oxygen on which H* is adsorbed (see Figure S5), and the reference for the removed oxygen is considered as H_2O-H_2. Positive strain values correspond to tensile strain, while negative values indicate compressive strain.

Moreover, ΔG_{H*} on $IrO_2(100)$ and $IrO_2(101)$ shows a monotonic increase in the adsorption strength when strain is changed from −5 to 5%, whereas ΔG_{H*} on $IrO_2(110)$ follows through a maximum located at −3% strain. Even though the H* adsorption strength varies according to a clear trend among different surfaces, there is no identifiable trend in $\Delta G_{O\text{-vacancy}}$. Interestingly, $\Delta G_{O\text{-vacancy}}$ on all of the considered surfaces reaches a maximum when changing the strain. The $\Delta G_{O\text{-vacancy}}$ on $IrO_2(100)$ increases slightly from 0.28 eV at −5% strain to 0.33 eV at both −4 and −3% strains and decreases when the strain is changed further from −3 to 5% varying in the range of 0.33 to −0.44 eV. On $IrO_2(101)$, the maximum $\Delta G_{O\text{-vacancy}}$ is 0.88 eV, which is located at 1% strain compared to 0.28 and 0.44 eV at −5 and 5% strains, respectively. In contrast to the other surfaces, $G_{O\text{-vacancy}}$ on $IrO_2(110)$ increases rapidly in the strain range of −5% (−1.13 eV) to 0% (0.71 eV) and reaches a maximum value of 1.02 eV at 3%. Additionally, $\Delta G_{O\text{-vacancy}}$ on $IrO_2(110)$ shows a much wider variation of 2.15 eV compared to 0.77 and 0.60 eV variations on $IrO_2(100)$ and $IrO_2(101)$, respectively.

Generally, as observed in the literature, ΔG_{H*} correlates positively (with a positive gradient) with $\Delta G_{O\text{-vacancy}}$.[35] Increasing $\Delta G_{O\text{-vacancy}}$ indicates an increase of bond strength between Ir and adjacent lattice O. Based on the bond order conservation, ΔG_{H*} will also be increased, indicating weaker H* adsorption on the lattice O. However, the correlation of ΔG_{H*} vs $\Delta G_{O\text{-vacancy}}$ in the presence of various strains shows an entirely different trend, as shown in Figure S6. The ΔG_{H*} vs $\Delta G_{O\text{-vacancy}}$ variation of $IrO_2(100)$ shows a positive gradient for the majority of strains, with a minor portion of negative gradient from −5 to −4% strains. Conversely, the −5 to 1% strain range shows negative gradients on $IrO_2(101)$, whereas the gradient changes from positive to negative and then again to positive values on $IrO_2(110)$ in the strain range of −5 to 5%.

Figure 4 and Table S4 show the effect of strain on the AEM and LOM overpotentials on the $IrO_2(110)$, $IrO_2(101)$, and

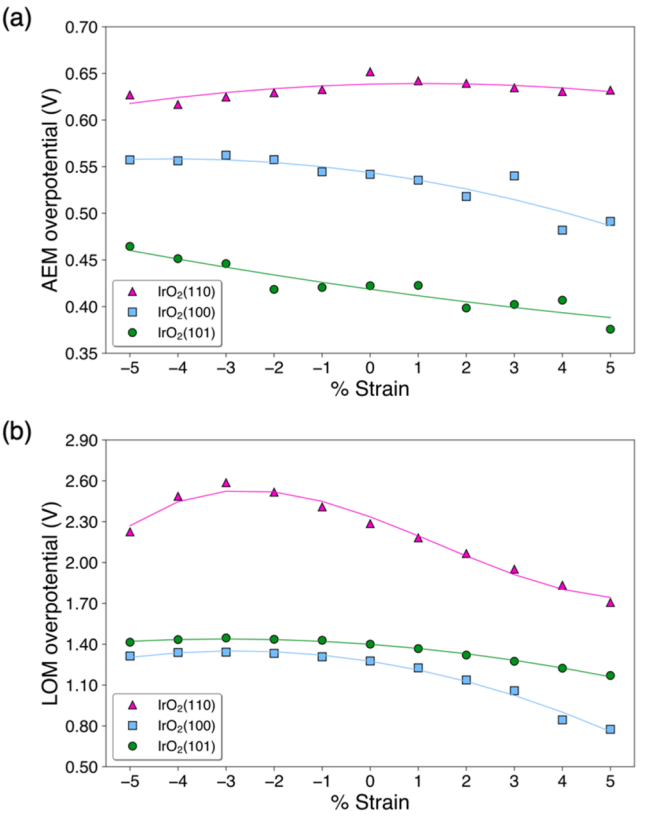

Figure 4. Effect of strain on the AEM and LOM overpotentials on IrO_2 surfaces under low coverage conditions. Effect of compressive and tensile strains on overpotential for (a) AEM and (b) LOM pathways across different surfaces of $IrO_2(110)$, $IrO_2(100)$, and $IrO_2(101)$ under low coverage conditions. Positive strain values correspond to tensile strain, while negative values indicate compressive strain.

$IrO_2(100)$ surfaces. Based on Figure 4a, the AEM overpotentials of unconstrained surfaces vary as $IrO_2(110)$ > $IrO_2(100)$ > $IrO_2(101)$, in agreement with previous studies.[29] This observed trend is valid for the entire range of compressive and tensile strains. 5% strained $IrO_2(101)$ showed the highest activity with a calculated OER overpotential of 0.38 V. Notably, the AEM overpotentials for all of the facets show narrower variations in the strain range of −5 to +5%, although some of the OER intermediates show a relatively wide range of variations with strain. AEM overpotentials of $IrO_2(110)$ remained almost unchanged, varying in the range of 0.62−0.65 V. The overpotentials of both $IrO_2(100)$ and $IrO_2(101)$ surfaces tend to decrease under compressive strain (−5 to 0%) and further decrease with increasing tensile strain (0−5%). Moreover, $IrO_2(100)$ and $IrO_2(101)$ show relatively higher overpotential variations in the ranges of 0.48−0.56 V and

https://doi.org/10.1021/acs.iecr.5c01104
Ind. Eng. Chem. Res. 2025, 64, 16531−16543

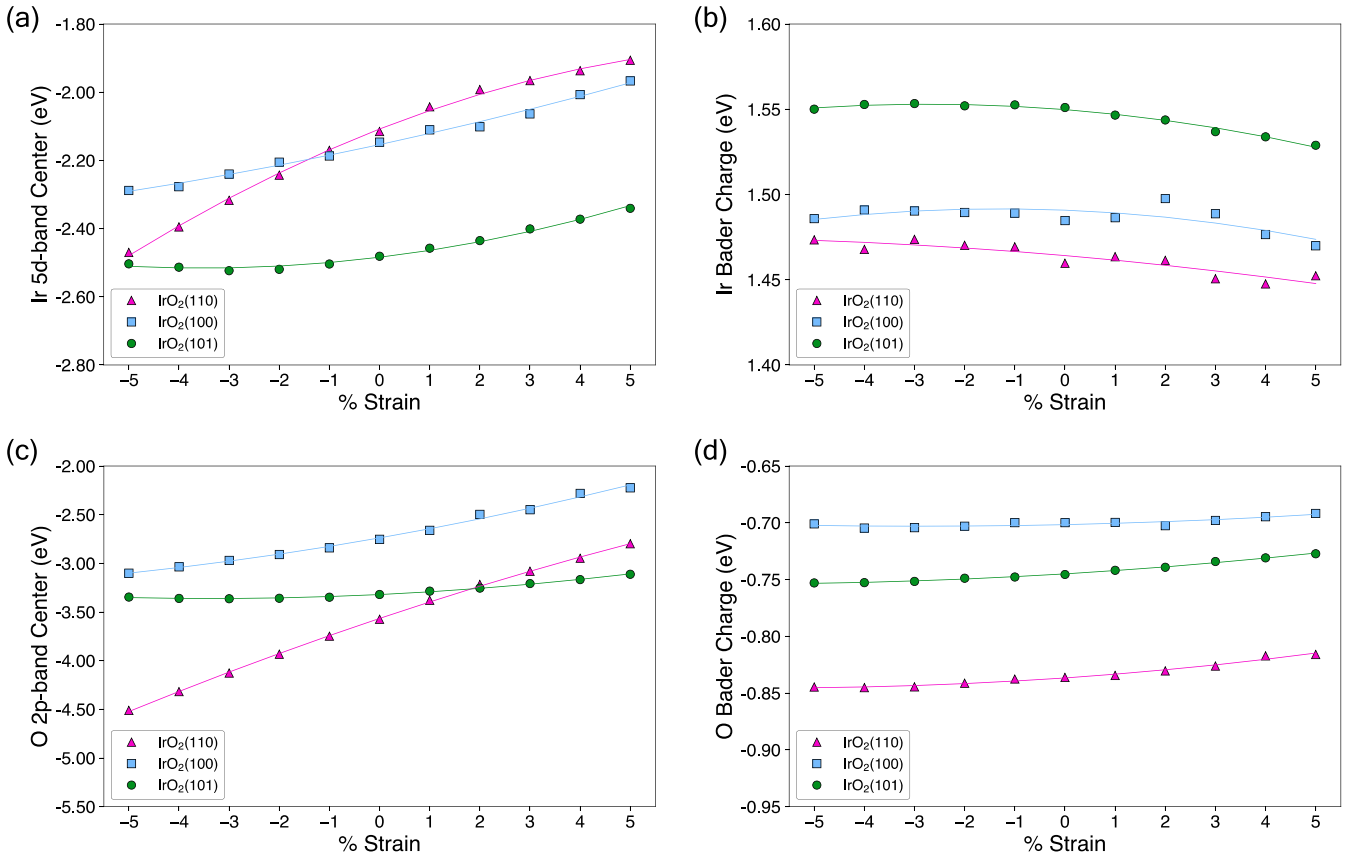

Figure 5. Effect of strain on the Ir 5d- and 2p-band centers and Bader charges of surface atoms on IrO_2. (a) 5d-band center, (b) Bader charge variation for the surface iridium (Ir) active sites, and (b) 2p-band center. (d) Bader charge variation for lattice oxygen (O) adjacent to the Ir active sites on different IrO_2 surfaces under varying strain conditions (%).

0.38−0.48 V, respectively. The potential-determining step of the AEM on $IrO_2(100)$ is the third step ($H_2O + O^* \rightarrow OOH^* + (H^+ + e^-)$) in the compressive range and 0% strain while it changes to fourth step ($OOH^* \rightarrow O_{2\,(g)} + * + (H^+ + e^-)$) in the tensile strain range. Similarly, the potential-determining step of the AEM changes from the third step to the fourth step on $IrO_2(101)$, but only occurs at 5% strain.

The LOM overpotentials are greater than 1 V in the considered strain range for all of the surfaces, except for 4% and 5% strains on $IrO_2(100)$, and considerably larger than their AEM overpotentials. Additionally, the LOM overpotentials varied as $IrO_2(110) > IrO_2(101) > IrO_2(100)$, and all the surfaces followed similar trends, reaching the maximum overpotential at −3% strain and decreasing further in the strain range of −2 to 5%. Moreover, it is observed that the decrease of overpotential is more predominant in the tensile strain range. On $IrO_2(110)$, the maximum LOM overpotential (at −3%) is more pronounced as it increases by 0.35 V from the overpotential values corresponding to −5% strain, though the overpotentials increase by only 0.03 V on the other two surfaces due to the equivalent increase of free energy of H* adsorption on $IrO_2(110)$ compared to $IrO_2(101)$ and $IrO_2(100)$. This is because the third step of LOM ($V_o + H_2O \rightarrow H^*_{\text{lattice-O}} + (H^+ + e^-)$) acts as the potential-determining step for all of the surfaces in the considered strain range due to the weak adsorption of H* on lattice O adjacent to Ir active sites. Moreover, $IrO_2(110)$ shows much higher LOM overpotentials in the range of 1.71−2.58 V compared to $IrO_2(101)$ (1.17−1.45 V) and $IrO_2(100)$ (0.78−1.34 V). Chaudhary et al. also observed a decreasing trend of LOM overpotentials in the strain range of −2 to 2% on the $IrO_2(110)$ surface,[7] in agreement with the current study.

3.3. Analysis of Strain on the Electronic Structure of IrO_2 Surfaces. To understand the origin of the strain effects, we investigated the electronic structure of the IrO_2 surfaces with varying strains by performing density of states (DOS) and Bader charge analyses. Figure 5 shows the band center (5d-band for Ir and 2p-band for O) and Bader charge variations in the surface Ir adsorption sites and lattice O adjacent to the considered Ir atom with strain on the IrO_2 surfaces. Additionally, Figure S7 shows the variations in the bandwidth for the aforementioned atoms with strain. It is clearly visible that the d-band centers of the Ir adsorption sites decrease, while the d-band widths of Ir increase with increasing compressive strain for $IrO_2(110)$ and $IrO_2(100)$. Notably, $IrO_2(101)$ is an exception to this observation due to the plateauing of the d-band centers in the compressive strain range, though their d-band widths align with the observed variation. Extending the trend to the tensile strain range, the d-band centers of Ir adsorption sites increase, and the d-band widths of Ir decrease when increasing the tensile strain on all the surfaces. The Bader charge of Ir, which indicates the oxidation state of Ir, remained almost the same in the compressive strain range, and slightly decreased by less than +0.03e under tensile strains. Chaudhari et al. also observed decreasing Ir Bader charge when increasing the applied lattice strain from −4 to 4% on $IrO_2(110)$.[7]

https://doi.org/10.1021/acs.iecr.5c01104
Ind. Eng. Chem. Res. 2025, 64, 16531−16543

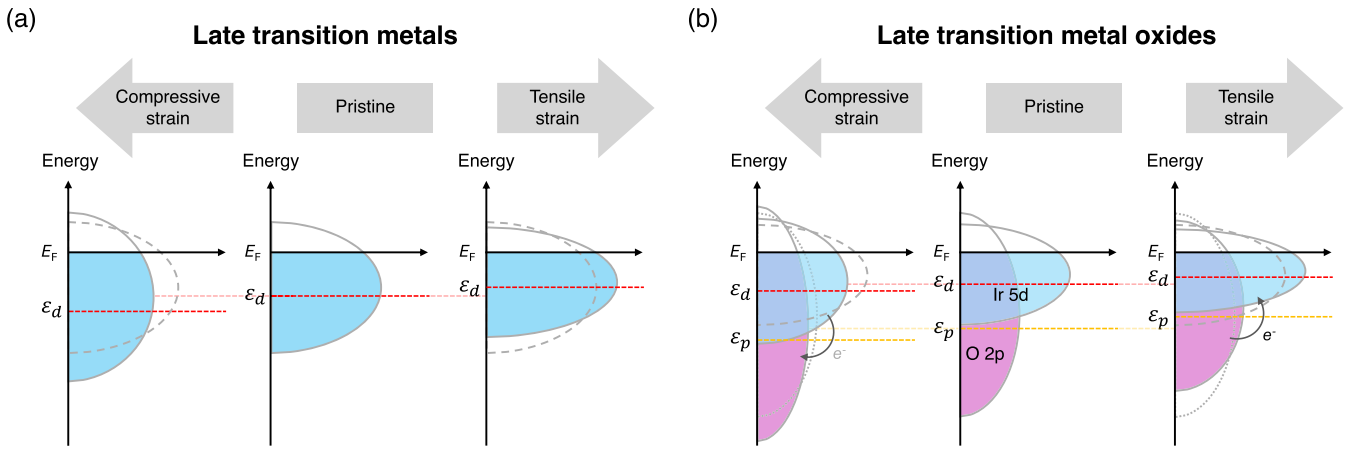

Figure 6. Comparison of the strain effects on the electronic structure of metal and metal oxides. (a) d-band variations of late transition metals. (b) d-band variations of surface Ir and 2p-band variations of adjacent lattice oxygen under compressive, unstrained, and tensile strains. The *x*-axis of each subfigure denotes the local density of states (DOS), while the *y*-axis denotes the energy relative to the Fermi level (E_F). ε_d represents the d-band center of a late transition metal or Ir, and ε_p represents the p-band center of adjacent lattice oxygen. The gray dashed lines in each strained subfigure show the DOS of the respective unstrained surface.

The effect of strain on transition metal surfaces is well established using the d-band model.[6,15] According to the d-band model, the position of the d-band center of a surface metal atom determines the strength of the metal−adsorbate interaction, and the d-band center can be modulated by the local coordination environment. Specifically, a decrease in coordination, that is, a reduction in the number of neighboring metal atoms, results in a narrower local bandwidth and an upshift of the d-band center for late transition metals with a d-band that is more than half-filled. For late transition metals (Figure 6a), the application of tensile strain lowers the coordination and results in a narrowing bandwidth and an upshift in the d-band center, leading to a stronger interaction with the adsorbates. However, the application of compressive strain to late transition metals has the opposite effect. As the coordination increases during compressive strain, a broadening of the bandwidth and a downshift in the d-band center result in a weaker interaction with the adsorbates.[6,15] Interestingly, we observed a trend similar to that of late transition metals for the *d*-band on surface Ir atom in IrO_2. Experimentally, downshifting of the d-band center of Ir was observed in Sr_2IrO_4 under compressive strains produced by anisotropic thermal expansions.[36] In addition to the metal d-band, the lattice O 2p-band also plays an important role in metal−oxide reactivity.[37−39] Our calculated 2p-band center and the 2p-bandwidth of the lattice O also show variations very similar to those of Ir active sites in the presence of strains, indicating that the effects of strain on both Ir and O on different surfaces are similar in nature. To further support this observation, the d-band center and width of Ir vary in a wider range, similar to the p-band center and width of lattice O on $IrO_2(110)$, though those variations are relatively narrower on $IrO_2(100)$ and $IrO_2(101)$ (see Figures 5a,c and S7). The Bader charges of lattice O (see Figure 5d) on all the surfaces tend to slightly increase in the tensile strain range, showing an opposite trend to Ir due to the requirement for maintaining the charge balance. This indicates that electron transfer occurs from lattice O to Ir atoms on the surface under tensile strains, resulting in lower covalency of the Ir−O bond. Interestingly, the observed charge transfer between Ir and O is relatively low in the considered strain range (Figure 5b,d). It is important to note that charge transfer phenomena, which are ubiquitous in reducible oxides like CeO_2, TiO_2, and MnO_x, can indeed dramatically alter the local electronic environment and reactivity. Moreover, in oxides, strain modulates both the electronic structure and the propensity for reduction, leading to local changes in valence and bonding. These effects are typically not captured in the d-band analogy of oxides. Figure 6b summarizes the effects of strain on the Ir 5d- and O 2p-bands, where charge transfer effects are minimal for the variations of the band properties.

3.4. Effect of Strain on Ir Vacancy Formation, Adsorption of OER Intermediates, and Overpotentials in the Presence of a Nearby Ir Vacancy under Low Coverage Conditions. Highly acidic environments with high oxidizing potentials under OER conditions result in slow dissolution of IrO_2 electrocatalysts, forming Ir vacancies on the IrO_2 surface.[40] Thus, we have evaluated the effect of strain on the favorability of the formation of Ir vacancies, which is a useful descriptor for predicting the stability of the catalyst surface.[37,41] It is important to note that the exact dissolution mechanism involving surface Ir atoms with different oxidation states and IrO_xH_y species still remains unclear.[42] Figure 7a shows the atomistic figures of Ir vacancies and adsorption sites adjacent to the formed Ir vacancies on selected IrO_2 surfaces, while Figure 7b shows the variations of Ir vacancy formation energy ($\Delta E_{Ir\text{-}vac}$) with varying strains on the considered IrO_2 surfaces. More positive values of $\Delta E_{Ir\text{-}vac}$ indicate a more endothermic nature of detaching an Ir atom from the surface, resulting in higher stability. $IrO_2(101)$ shows the highest $\Delta E_{Ir\text{-}vac}$, followed by $IrO_2(100)$, whereas Ir vacancy formation is most favorable on $IrO_2(110)$ in the entire strain range. $\Delta E_{Ir\text{-}vac}$ reaches a maximum on all the surfaces, but the position of the maximum varies depending on the surface. $IrO_2(110)$ shows a wider variation of $\Delta E_{Ir\text{-}vac}$ and reaches a maximum at 2 and 3% strain. Chaudhary et al. observed a similar trend in increasing free energy of Ir vacancy formation on $IrO_2(110)$ in the strain range of −4 to 4%.[7] Additionally, the $IrO_2(110)$ surface shows a significant decrease in Ir vacancy formation energies with increasing compressive strains, indicating lower catalyst stability under highly compressive strains. The maximum value of 4.11 eV is attained for $\Delta E_{Ir\text{-}vac}$ in the

https://doi.org/10.1021/acs.iecr.5c01104
Ind. Eng. Chem. Res. 2025, 64, 16531−16543

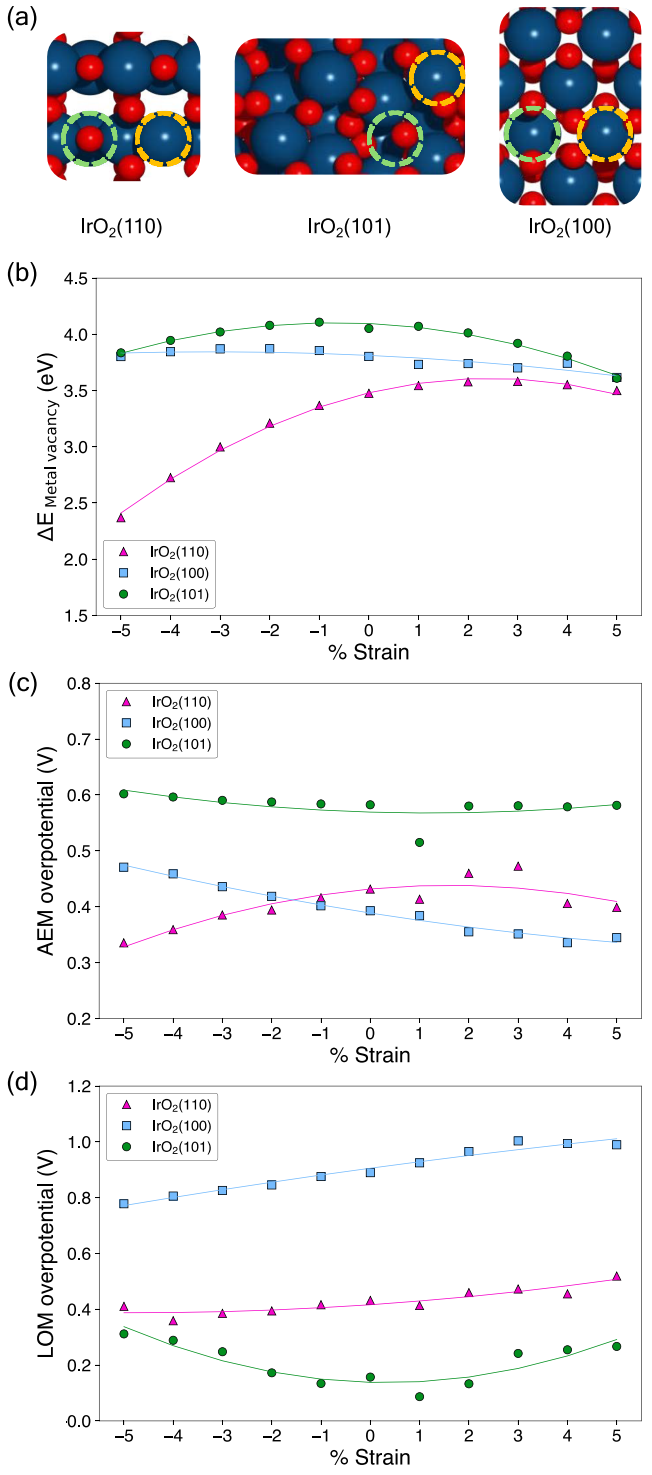

Figure 7. Effect of strain on metal vacancy formation on IrO_2 and the activity in the presence of a nearby Ir vacancy. (a) Atomistic figures showing Ir vacancies (light green dashed circle) and considered Ir adsorption sites of the OER intermediates (yellow dashed circle) on the IrO_2 surfaces. The effects of strain on (b) metal vacancy formation energy and overpotentials for (c) AEM and (d) LOM pathways across different surfaces of $IrO_2(110)$, $IrO_2(100)$, and $IrO_2(101)$ in the presence of a nearby Ir vacancy.

presence of −1% strain on $IrO_2(101)$, while surfaces with −2 and −3% resulted in the maximum value of 3.87 eV on the $IrO_2(100)$ surface. Subsequently, we performed adsorption energy analysis for the AEM and LOM intermediates (Figure S8) on the surfaces with Ir vacancies, followed by the evaluation of their AEM and LOM overpotentials, as shown in Figure 7c,d. Similar to the variations of the adsorption strengths of the OER intermediates observed in Figure 2 under low coverage conditions, ΔG_{O^*}, ΔG_{OH^*}, and ΔG_{OOH^*} vary according to the adsorption strength trend of $IrO_2(110)$ > $IrO_2(100)$ > $IrO_2(101)$ in the presence of a nearby Ir vacancy. However, the adsorption strengths of those intermediates become weaker in the presence of a nearby Ir vacancy on all the considered surfaces compared to adsorption under pristine low coverage conditions with the respective strain. Moreover, adsorption of all the AEM intermediates on $IrO_2(101)$ became more favorable with strain changing from −5 to 5%, whereas the free energy of adsorption trends goes through a slight minimum on $IrO_2(100)$. ΔG_{O^*} and ΔG_{OH^*} become slightly unfavorable on $IrO_2(110)$ in the strain range from −5 to 5%, although ΔG_{OOH^*} remains almost unchanged. ΔG_{H^*} becomes more favorable in the presence of a nearby Ir vacancy on all the surfaces compared to adsorption under pristine low coverage conditions, in contrast to ΔG_{O^*}, ΔG_{OH^*}, and ΔG_{OOH^*}. Moreover, $IrO_2(100)$ shows the highest favorability for H* adsorption on adjacent lattice O under both low coverage and in the presence of a nearby Ir vacancy. Interestingly, H* adsorption on adjacent lattice O is stronger on $IrO_2(110)$ compared to $IrO_2(101)$, in contrast to the trend observed under low coverage conditions.

Based on Figure 7c,d, the $IrO_2(110)$ and $IrO_2(100)$ surfaces show reduced AEM overpotentials in the presence of a nearby Ir vacancy compared to the pristine surface under low coverage conditions with varying strains from −5 to 5%. The AEM overpotential of the $IrO_2(110)$−Ir vacancy is lowest at −5% strain (0.34 V) and increases to reach a maximum at 3% strain (0.47 V) compared to the narrow range of variation between 0.62 and 0.65 V under pristine low coverage conditions. However, the AEM overpotentials of the $IrO_2(100)$−Ir vacancy show a monotonically decreasing trend from 0.47 V at −5% strain to 0.34 V at 5% strain. Notably, the AEM overpotentials of $IrO_2(101)$ are increased in the presence of a nearby Ir vacancy compared to those under pristine low coverage conditions and varied in a narrow range of 0.58−0.6 V except for the surface under 1% strain. Considering the LOM overpotentials in the presence of an Ir vacancy, unstrained $IrO_2(110)$ and $IrO_2(101)$ showed drastically reduced LOM overpotentials compared to pristine unstrained low coverage conditions, although unstrained $IrO_2(100)$ showed a limited improvement. This is evident by unstrained pristine $IrO_2(110)$ having an LOM overpotential of 2.29 V compared to that of 0.43 V in the $IrO_2(110)$−Ir vacancy (1.86 V improvement) and an LOM overpotential of 1.40 V on unstrained pristine $IrO_2(101)$ compared to that of 0.16 V on the $IrO_2(101)$−Ir vacancy (1.24 V improvement). This can be attributed to the change in the potential-determining step due to stronger H* adsorption or weakening of the adsorption of O*, OH*, and OOH*. $IrO_2(100)$ shows the least improvement under unconstrained conditions by reducing the LOM overpotential from 1.28 to 0.89 V (0.39 V improvement). Introducing strain resulted in slightly more favorable conditions, such as the lowest overpotentials of 0.36 V at −4% strain on $IrO_2(110)$, 0.09 V at 1% strain on $IrO_2(101)$, and 0.78 V at −5% strain on $IrO_2(100)$ in the presence of a nearby Ir vacancy. Overall, the higher LOM activity originates from the presence of a nearby Ir vacancy, and the strain further modifies the activity.

https://doi.org/10.1021/acs.iecr.5c01104
Ind. Eng. Chem. Res. 2025, 64, 16531−16543

3.5. Effects of Strain on Adsorption of OER Intermediates and OER Overpotentials under High Surface Oxygen Coverage Conditions. Since the coverage of reaction intermediates significantly influences the local environment of the active site,[29,43,44] we incorporated the coverage effects by considering high surface oxygen coverage, which was shown to be the most stable under OER on IrO_2.[29] It is important to note that incorporating high coverage would result in through-space attractions and repulsions, which result in further complexity in evaluating only strain effects. Figure S9 shows the adsorption free energy trends of the AEM- and LOM-based reaction intermediates under high coverage conditions. High surface oxygen coverages were simulated by adding one O* species adjacent to the active site on the CUS of $IrO_2(110)$ and three O* species on the $IrO_2(100)$ and $IrO_2(101)$ surfaces, as shown in Figure 8a. The adsorption strengths of all AEM reaction intermediates of O*, OH*, and OOH* follow the previously observed trend as $IrO_2(110)$ > $IrO_2(100)$ > $IrO_2(101)$ for all the strains. Free energies of the AEM reaction intermediates show much lower variations under high coverage conditions (variations of 0.13−0.16 eV) compared to previously observed pristine low coverage conditions (variations of 0.28−0.34 eV) on $IrO_2(100)$. Additionally, all the AEM reaction intermediates on the considered surfaces show slightly decreasing favorability to adsorb when increasing the compressive strain (from −1 to −5% strain). Increasing the tensile strain from 1 to 5% results in increasing the adsorption strength of all AEM intermediates on $IrO_2(101)$ and OOH* on $IrO_2(110)$, while others are almost insensitive to tensile strain under high coverage conditions. Considering H* adsorption on the nearby lattice of O, it becomes more favorable when increasing the tensile strain for all the surfaces.

Figure 8b,c shows the variations of AEM and LOM overpotentials under high surface oxygen coverage conditions with strain. $IrO_2(101)$ shows the highest AEM activity in the strain range of −5 to 5%, similar to trends that we observed under low coverage conditions. The AEM overpotentials of $IrO_2(110)$ and $IrO_2(100)$ vary in a wider range with strain under high coverage conditions compared to low coverage conditions. For instance, the overpotential on $IrO_2(110)$ varies in the range of 0.47 to 0.68 V under high coverage conditions, in contrast to the almost unchanged variation of overpotential (0.62 to 0.65 V) under low coverage. The AEM overpotential tends to increase with strain in the range of −5 to 5% on $IrO_2(110)$, whereas it decreases to reach a minimum of 0.40 V overpotential at 2% strain and then increases on $IrO_2(100)$. Considering the LOM overpotentials under high surface coverage conditions on unconstrained $IrO_2(110)$, it remains at 2.15 V without showing much difference compared to 2.29 V under pristine low coverage conditions due to less stable H adsorption on lattice oxygen in both cases. Moreover, the LOM overpotential of $IrO_2(110)$ decreases when the strain is increased from −2 to 5% and reaches 1.61 V at 5% strain. This variation suggests that the LOM mechanism is not active on $IrO_2(110)$ in the considered strain range. Additionally, note that the LOM overpotential values of $IrO_2(110)$ in the strain range of −5 to −3% are not available due to the movement of H* adsorbed on lattice oxygen to O* adsorbed on Ir active sites during the optimization. However, $IrO_2(100)$ and $IrO_2(101)$ show considerably lower LOM overpotentials compared to low coverage conditions in the considered strain range, including even 0% strain. The LOM overpotentials of

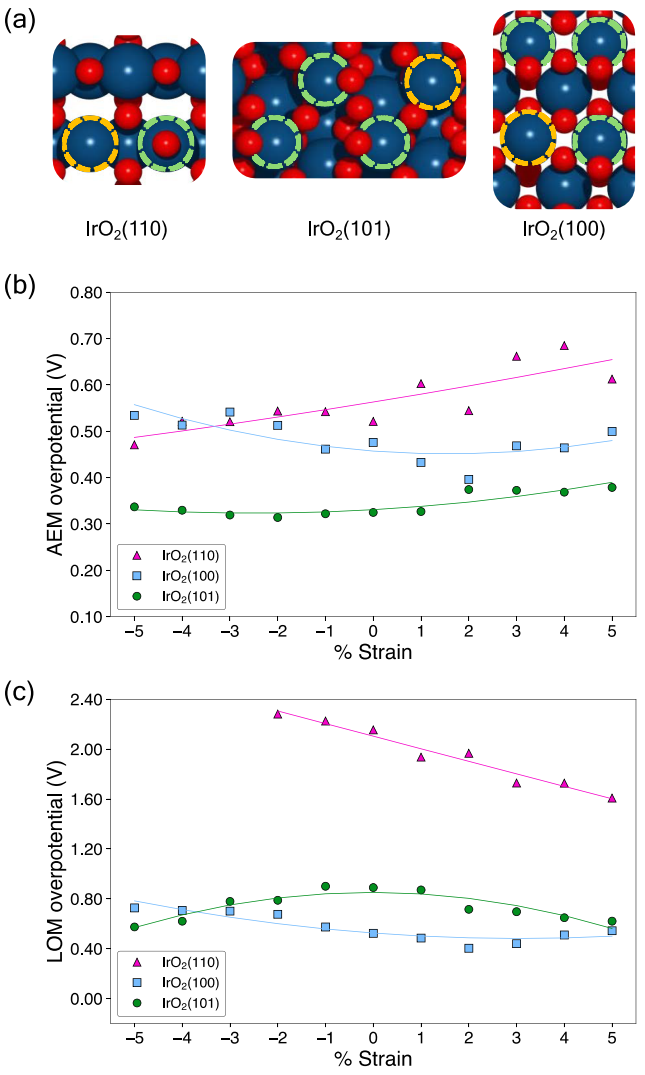

Figure 8. Effects of strain on the AEM and LOM overpotentials of IrO_2 under high coverage conditions. (a) Atomistic figures showing high surface oxygen coverage on IrO_2 surfaces. Yellow dashed circles represent the Ir adsorption sites of the OER intermediates, while light green dashed circles represent oxygen-covered surface Ir sites. Effect of compressive and tensile strains on the overpotential for (b) AEM and (c) LOM pathways across different surfaces of $IrO_2(110)$, $IrO_2(100)$, and $IrO_2(101)$ under high surface oxygen coverage conditions. Note that H* adsorption on lattice O was observed to be unstable in the strain range of −5 to −3% on $IrO_2(110)$.

$IrO_2(100)$ decrease from 0.73 V at −5% strain to the lowest of 0.40 V at 2% strain and increase to 0.54 V at 5% strain. These low overpotential values reveal that the LOM mechanism is competitive with the AEM mechanism in the tensile range, which shows overpotentials in the range of 0.40−0.50 V on $IrO_2(100)$ at high coverage conditions. The LOM overpotentials of $IrO_2(101)$ indicate that the LOM mechanism becomes relatively more favorable with highly compressive (overpotential of 0.57 V at −5%) and highly tensile strains (overpotential of 0.62 V at 5%) compared to the nonstrained (overpotential of 0.89 V) surface, although the AEM overpotentials vary in a slightly lower range of 0.31−0.38 V under high surface coverage conditions. These observations clearly show that the effects of strain can be drastically different under low coverage and high surface coverage conditions,

https://doi.org/10.1021/acs.iecr.5c01104
Ind. Eng. Chem. Res. 2025, 64, 16531−16543

potentially due to through-space interactions, indicating the necessity to model more realistic conditions.

Overall, this study primarily focuses on evaluating the effects of strain on the thermodynamics of OER intermediates using standard DFT. We showed that biaxial strain on different IrO_2 surfaces can considerably alter the adsorption of OER intermediates, thereby altering the OER activity and stability. However, it is important to note that electrified interfaces that facilitate the adsorption of reaction intermediates and the progression of the reaction are far more complex and dynamic. This complexity arises from various phenomena, including the solvation of adsorbed species, interfacial electric field effects, local pH variations, adsorption of ions, etc. These factors can either weaken or strengthen the bonds between the OER intermediates and the surface, as well as modify the electronic properties of IrO_2 surfaces. Moreover, it is important to recognize that the OER kinetics can also be affected by strain. Analyzing these phenomena and their kinetic effects under strain would require performing detailed constant potential barrier calculations and establishing microkinetic models.

4. CONCLUSIONS

In conclusion, we performed a systematic analysis of the effects of surface biaxial compressive and tensile strains on IrO_2 surfaces to understand the role of strain on the adsorption of key OER surface intermediates, the OER activity based on both AEM and LOM mechanisms, and the surface electronic structure. Our results showed that the response in adsorption free energies of OER intermediates due to strain significantly varies for the considered surfaces. As a result, different trends in AEM and LOM activities were observed. Our density of states calculations revealed that the d-band center of surface Ir increases with increasing strain from −5 to 5%, while the d-bandwidth decreases, similar to the trends established on late transition metal surfaces. Interestingly, we observed a similar trend for the 2p-band center and p-bandwidth of the adjacent lattice oxygen. The $IrO_2(110)$ surface showed the largest decrease in Ir vacancy formation energies with increasing compressive strain, indicating lower catalyst stability under compressive strain. The LOM overpotentials on the $IrO_2(110)$ and $IrO_2(101)$ surfaces in the presence of a nearby Ir vacancy were significantly lower, but that also resulted in lower stability. Our high surface oxygen coverage calculations revealed that LOM becomes as active as AEM under tensile strain on $IrO_2(100)$. Overall, our findings provide crucial theoretical insights into the effects of strain on IrO_2, expanding the current understanding and eventually leading to the development of more efficient catalysts for water electrolyzers by strain engineering.

■ ASSOCIATED CONTENT

Data Availability Statement

Data collected in support of the findings are available in the main text and Supporting Information. Moreover, the optimized DFT structures and data can be accessed using the link https://github.com/gunasooriya-lab/manuscripts.

Supporting Information

The Supporting Information is available free of charge at https://pubs.acs.org/doi/10.1021/acs.iecr.5c01104.

Computational methods benchmarking; bulk structure and considered facets of IrO_2 (Figure S1); variation of average layer distance with applied strain on the $IrO_2(110)$, $IrO_2(101)$, and $IrO_2(100)$ surfaces (Figure S2); atomistic figures of OH* adsorption on IrO_2 surfaces (Figure S3); linear scaling relations between free energies of OER intermediates with strain on IrO_2 under low coverage conditions (Figure S4); atomistic figures of H* adsorption and O vacancies on the IrO_2 surfaces (Figure S5); variation of free energy of H* adsorption (ΔG_{H^*}) on lattice O and free energy of oxygen vacancy formation ($\Delta G_{O\text{-vacancy}}$) on the $IrO_2(110)$, $IrO_2(101)$, and $IrO_2(100)$ surfaces with strain (Figure S6); variations of the Ir 5d and lattice O 2p-band widths with strain on the $IrO_2(110)$, $IrO_2(101)$, and $IrO_2(100)$ surfaces (Figure S7); strain effects on the adsorption of key OER intermediates in the presence of a nearby Ir vacancy (Figure S8); strain effects on the adsorption of key OER intermediates under surface oxygen coverage conditions (Figure S9); energy cut-off and kpoints convergence (Table S1); CPU time utilized for convergence calculations (Table S2); variations of average layer distance with applied strain (Table S3); variations of adsorption free energies of OER intermediates under low coverage (Table S4); variations of free energies of oxygen vacancy formation (Table S5); variations of the properties of density of states (DOS) (Table S6); variations of the Bader charges of surface Ir active site and lattice O (Table S7); variations of Ir vacancy formation energies (Table S8); variations of adsorption free energies of OER intermediates in the prescence of a nearby vacancy (Table S9); variations of adsorption free energies of OER intermediates under high oxygen coverage (Table S10) (PDF)

■ AUTHOR INFORMATION

Corresponding Author

G. T. Kasun Kalhara Gunasooriya − *School of Sustainable Chemical, Biological and Materials Engineering, University of Oklahoma, Norman, Oklahoma 73019, United States;* orcid.org/0000-0003-1258-7841; Email: kasun.gunasooriya@ou.edu

Authors

Erum Hassan − *School of Sustainable Chemical, Biological and Materials Engineering, University of Oklahoma, Norman, Oklahoma 73019, United States*

S. A. Keishana Navodye − *School of Sustainable Chemical, Biological and Materials Engineering, University of Oklahoma, Norman, Oklahoma 73019, United States;* orcid.org/0009-0008-4121-516X

Complete contact information is available at: https://pubs.acs.org/10.1021/acs.iecr.5c01104

Author Contributions

†E.H. and S.A.K.N. contributed equally to this work.

Notes

The authors declare no competing financial interest.

■ ACKNOWLEDGMENTS

Computing for this project was performed at the OU Supercomputing Center for Education & Research (OSCER) at the University of Oklahoma. G.T.K.K.G. gratefully acknowledges start-up funding support from the School of Sustainable Chemical, Biological and Materials Engineering, University of

Oklahoma and financial support by the University of Oklahoma Libraries' Open Access Fund.

REFERENCES

(1) Shih, A. J.; Monteiro, M. C. O.; Dattila, F.; Pavesi, D.; Philips, M.; Da Silva, A. H. M.; Vos, R. E.; Ojha, K.; Park, S.; Van Der Heijden, O.; Marcandalli, G.; Goyal, A.; Villalba, M.; Chen, X.; Gunasooriya, G. T. K. K.; McCrum, I.; Mom, R.; López, N.; Koper, M. T. M. Water Electrolysis. *Nat. Rev. Methods Primers* **2022**, *2* (1), No. 84.

(2) Seh, Z. W.; Kibsgaard, J.; Dickens, C. F.; Chorkendorff, I.; Nørskov, J. K.; Jaramillo, T. F. Combining Theory and Experiment in Electrocatalysis: Insights into Materials Design. *Science* **2017**, *355* (6321), No. eaad4998.

(3) Ayers, K. E.; Anderson, E. B.; Capuano, C.; Carter, B.; Dalton, L.; Hanlon, G.; Manco, J.; Niedzwiecki, M. Research Advances towards Low Cost, High Efficiency PEM Electrolysis. *ECS Trans.* **2010**, *33* (1), 3−15.

(4) Hou, Z.; Cui, C.; Li, Y.; Gao, Y.; Zhu, D.; Gu, Y.; Pan, G.; Zhu, Y.; Zhang, T. Lattice-Strain Engineering for Heterogenous Electrocatalytic Oxygen Evolution Reaction. *Adv. Mater.* **2023**, *35* (39), No. 2209876.

(5) Yang, X.; Wang, Y.; Tong, X.; Yang, N. Strain Engineering in Electrocatalysts: Fundamentals, Progress, and Perspectives. *Adv. Energy Mater.* **2022**, *12* (5), No. 2102261.

(6) Mavrikakis, M.; Hammer, B.; Nørskov, J. K. Effect of Strain on the Reactivity of Metal Surfaces. *Phys. Rev. Lett.* **1998**, *81* (13), 2819−2822.

(7) Chaudhary, P.; Zagalskaya, A.; Over, H.; Alexandrov, V. Strain-Dependent Activity-Stability Relations in RuO_2 and IrO_2 Oxygen Evolution Catalysts. *ChemElectroChem* **2024**, *11* (1), No. e202300659.

(8) Parks, V. J.; Durelli, A. J. On the Definitions of Strain and Their Use in Large-Strain Analysis. *Exp. Mech.* **1967**, *7* (6), 279−280.

(9) Feng, Z.; Dai, C.; Zhang, Z.; Lei, X.; Mu, W.; Guo, R.; Liu, X.; You, J. The Role of Strain in Oxygen Evolution Reaction. *J. Energy Chem.* **2024**, *93*, 322−344.

(10) Dayeh, S. A.; Tang, W.; Boioli, F.; Kavanagh, K. L.; Zheng, H.; Wang, J.; Mack, N. H.; Swadener, G.; Huang, J. Y.; Miglio, L.; Tu, K.-N.; Picraux, S. T. Direct Measurement of Coherency Limits for Strain Relaxation in Heteroepitaxial Core/Shell Nanowires. *Nano Lett.* **2013**, *13* (5), 1869−1876.

(11) Strasser, P.; Koh, S.; Anniyev, T.; Greeley, J.; More, K.; Yu, C.; Liu, Z.; Kaya, S.; Nordlund, D.; Ogasawara, H.; Toney, M. F.; Nilsson, A. Lattice-Strain Control of the Activity in Dealloyed Core−Shell Fuel Cell Catalysts. *Nature Chem.* **2010**, *2* (6), 454−460.

(12) Zhang, X.; Lu, G. Computational Design of Core/Shell Nanoparticles for Oxygen Reduction Reactions. *J. Phys. Chem. Lett.* **2014**, *5* (2), 292−297.

(13) Liu, J.; Zhang, J. Nanointerface Chemistry: Lattice-Mismatch-Directed Synthesis and Application of Hybrid Nanocrystals. *Chem. Rev.* **2020**, *120* (4), 2123−2170.

(14) Tan, C.; Chen, J.; Wu, X.-J.; Zhang, H. Epitaxial Growth of Hybrid Nanostructures. *Nat. Rev. Mater.* **2018**, *3* (2), No. 17089.

(15) Luo, M.; Guo, S. Strain-Controlled Electrocatalysis on Multimetallic Nanomaterials. *Nat. Rev. Mater.* **2017**, *2* (11), No. 17059.

(16) Meng, G.; Sun, W.; Mon, A. A.; Wu, X.; Xia, L.; Han, A.; Wang, Y.; Zhuang, Z.; Liu, J.; Wang, D.; Li, Y. Strain Regulation to Optimize the Acidic Water Oxidation Performance of Atomic-Layer IrO_x. *Adv. Mater.* **2019**, *31* (37), No. 1903616.

(17) Sun, W.; Wang, Z.; Zaman, W. Q.; Zhou, Z.; Cao, L.; Gong, X.-Q.; Yang, J. Effect of Lattice Strain on the Electro-Catalytic Activity of IrO_2 for Water Splitting. *Chem. Commun.* **2018**, *54* (8), 996−999.

(18) Hao, S.; Sheng, H.; Liu, M.; Huang, J.; Zheng, G.; Zhang, F.; Liu, X.; Su, Z.; Hu, J.; Qian, Y.; Zhou, L.; He, Y.; Song, B.; Lei, L.; Zhang, X.; Jin, S. Torsion Strained Iridium Oxide for Efficient Acidic Water Oxidation in Proton Exchange Membrane Electrolyzers. *Nat. Nanotechnol.* **2021**, *16* (12), 1371−1377.

(19) Wu, X.; Hao, S.; He, Y.; Lei, L.; Zhang, X. Bi-Directional Strains Increase the Performance of Iridium Oxide Nanoparticles towards the Acidic Oxygen Evolution Reaction in Proton Exchange Membrane Electrolyzers. *Inorg. Chem. Front.* **2023**, *10* (23), 6892−6900.

(20) Su, H.; Yang, C.; Liu, M.; Zhang, X.; Zhou, W.; Zhang, Y.; Zheng, K.; Lian, S.; Liu, Q. Tensile Straining of Iridium Sites in Manganese Oxides for Proton-Exchange Membrane Water Electrolysers. *Nat. Commun.* **2024**, *15* (1), No. 95.

(21) Perdew, J. P.; Burke, K.; Ernzerhof, M. Generalized Gradient Approximation Made Simple. *Phys. Rev. Lett.* **1996**, *77* (18), 3865−3868.

(22) Kresse, G.; Furthmüller, J. Efficient Iterative Schemes for *Ab Initio* Total-Energy Calculations Using a Plane-Wave Basis Set. *Phys. Rev. B* **1996**, *54* (16), 11169−11186.

(23) Kresse, G.; Furthmüller, J. Efficiency of Ab-Initio Total Energy Calculations for Metals and Semiconductors Using a Plane-Wave Basis Set. *Comput. Mater. Sci.* **1996**, *6* (1), 15−50.

(24) Ong, S. P.; Richards, W. D.; Jain, A.; Hautier, G.; Kocher, M.; Cholia, S.; Gunter, D.; Chevrier, V. L.; Persson, K. A.; Ceder, G. Python Materials Genomics (Pymatgen): A Robust, Open-Source Python Library for Materials Analysis. *Comput. Mater. Sci.* **2013**, *68*, 314−319.

(25) Hjorth Larsen, A.; Jørgen Mortensen, J.; Blomqvist, J.; Castelli, I. E.; Christensen, R.; Dułak, M.; Friis, J.; Groves, M. N.; Hammer, B.; Hargus, C.; Hermes, E. D.; Jennings, P. C.; Bjerre Jensen, P.; Kermode, J.; Kitchin, J. R.; Leonhard Kolsbjerg, E.; Kubal, J.; Kaasbjerg, K.; Lysgaard, S.; Bergmann Maronsson, J.; Maxson, T.; Olsen, T.; Pastewka, L.; Peterson, A.; Rostgaard, C.; Schiøtz, J.; Schütt, O.; Strange, M.; Thygesen, K. S.; Vegge, T.; Vilhelmsen, L.; Walter, M.; Zeng, Z.; Jacobsen, K. W. The Atomic Simulation Environment—a Python Library for Working with Atoms. *J. Phys.:Condens. Matter* **2017**, *29* (27), No. 273002.

(26) Henkelman, G.; Arnaldsson, A.; Jónsson, H. A Fast and Robust Algorithm for Bader Decomposition of Charge Density. *Comput. Mater. Sci.* **2006**, *36* (3), 354−360.

(27) Nørskov, J. K.; Rossmeisl, J.; Logadottir, A.; Lindqvist, L.; Kitchin, J. R.; Bligaard, T.; Jónsson, H. Origin of the Overpotential for Oxygen Reduction at a Fuel-Cell Cathode. *J. Phys. Chem. B* **2004**, *108* (46), 17886−17892.

(28) Navodye, S. A. K.; Gunasooriya, G. T. K. K. Acid Electrolyte Anions Adsorption Effects on IrO2 Electrocatalysts for Oxygen Evolution Reaction. *J. Phys. Chem. C* **2024**, *128* (14), 6041−6052.

(29) Gunasooriya, G. T. K. K.; Nørskov, J. K. Analysis of Acid-Stable and Active Oxides for the Oxygen Evolution Reaction. *ACS Energy Lett.* **2020**, *5* (12), 3778−3787.

(30) Matz, O.; Calatayud, M. Periodic DFT Study of Rutile IrO2: Surface Reactivity and Catechol Adsorption. *J. Phys. Chem. C* **2017**, *121* (24), 13135−13143.

(31) Ocampo-Restrepo, V. K.; Vijay, S.; Gunasooriya, G. T. K. K.; Nørskov, J. K. Characterization of Adsorption Sites on IrO_2 *via* Temperature Programmed O_2 Desorption Simulations. *Phys. Chem. Chem. Phys.* **2024**, *26* (24), 17396−17404.

(32) Wang, L.; Stoerzinger, K. A.; Chang, L.; Yin, X.; Li, Y.; Tang, C. S.; Jia, E.; Bowden, M. E.; Yang, Z.; Abdelsamie, A.; You, L.; Guo, R.; Chen, J.; Rusydi, A.; Wang, J.; Chambers, S. A.; Du, Y. Strain Effect on Oxygen Evolution Reaction Activity of Epitaxial $NdNiO_3$ Thin Films. *ACS Appl. Mater. Interfaces* **2019**, *11* (13), 12941−12947.

(33) Meyer, T. L.; Jiang, L.; Park, S.; Egami, T.; Lee, H. N. Strain-Relaxation and Critical Thickness of Epitaxial La1.85Sr0.15CuO4 Films. *APL Mater.* **2015**, *3* (12), No. 126102.

(34) Keishana Navodye, S. A.; Gunasooriya, G. T. K. K. Analysis of Tin Oxide Supported Transition Metal Single-Atom Catalysts for Oxygen Evolution Reaction. *J. Mater. Chem. A* **2025**, *13*, 22093−22108.

(35) Theofanidis, S. A.; Gunasooriya, G. T. K. K.; Itskou, I.; Tasioula, M.; Lemonidou, A. A. On-purpose Ethylene Production via CO_2 -assisted Ethane Oxidative Dehydrogenation: Selectivity Control

https://doi.org/10.1021/acs.iecr.5c01104
Ind. Eng. Chem. Res. 2025, 64, 16531−16543

of Iron Oxide Catalysts. *ChemCatChem* **2022**, *14* (14), No. e202200032.
(36) Du, Y.; Xie, F.; Lu, M.; Lv, R.; Liu, W.; Yan, Y.; Yan, S.; Zou, Z. Continuous Strain Tuning of Oxygen Evolution Catalysts with Anisotropic Thermal Expansion. *Nat. Commun.* **2024**, *15* (1), No. 1780.
(37) Lu, B.; Wahl, C.; Dos Reis, R.; Edgington, J.; Lu, X. K.; Li, R.; Sweers, M. E.; Ruggiero, B.; Gunasooriya, G. T. K. K.; Dravid, V.; Seitz, L. C. Key Role of Paracrystalline Motifs on Iridium Oxide Surfaces for Acidic Water Oxidation. *Nat. Catal.* **2024**, *7* (8), 868−877.
(38) Grimaud, A.; Diaz-Morales, O.; Han, B.; Hong, W. T.; Lee, Y.-L.; Giordano, L.; Stoerzinger, K. A.; Koper, M. T. M.; Shao-Horn, Y. Activating Lattice Oxygen Redox Reactions in Metal Oxides to Catalyse Oxygen Evolution. *Nat. Chem.* **2017**, *9* (5), 457−465.
(39) Suntivich, J.; May, K. J.; Gasteiger, H. A.; Goodenough, J. B.; Shao-Horn, Y. A Perovskite Oxide Optimized for Oxygen Evolution Catalysis from Molecular Orbital Principles. *Science* **2011**, *334* (6061), 1383−1385.
(40) Geiger, S.; Kasian, O.; Shrestha, B. R.; Mingers, A. M.; Mayrhofer, K. J. J.; Cherevko, S. Activity and Stability of Electrochemically and Thermally Treated Iridium for the Oxygen Evolution Reaction. *J. Electrochem. Soc.* **2016**, *163* (11), F3132−F3138.
(41) Raman, A. S.; Vojvodic, A. Providing Atomistic Insights into the Dissolution of Rutile Oxides in Electrocatalytic Water Splitting. *J. Phys. Chem. C* **2022**, *126* (2), 922−932.
(42) Lončar, A.; Escalera-López, D.; Cherevko, S.; Hodnik, N. Inter-Relationships between Oxygen Evolution and Iridium Dissolution Mechanisms. *Angew. Chem., Int. Ed.* **2022**, *61* (14), No. e202114437.
(43) Man, I. C.; Su, H.; Calle-Vallejo, F.; Hansen, H. A.; Martínez, J. I.; Inoglu, N. G.; Kitchin, J.; Jaramillo, T. F.; Nørskov, J. K.; Rossmeisl, J. Universality in Oxygen Evolution Electrocatalysis on Oxide Surfaces. *ChemCatChem* **2011**, *3* (7), 1159−1165.
(44) De Vrieze, J. E.; Gunasooriya, G. K. K. K.; Thybaut, J. W.; Saeys, M. Operando Computational Catalysis: Shape, Structure, and Coverage under Reaction Conditions. *Curr. Opin. Chem. Eng.* **2019**, *23*, 85−91.

https://doi.org/10.1021/acs.iecr.5c01104
Ind. Eng. Chem. Res. 2025, 64, 16531−16543